WILEY | Hindawi

Research Article

Understanding of Long-Term CO$_2$-Brine-Rock Geochemical Reactions Using Numerical Modeling and Natural Analogue Study

Huixing Zhu (ID),[1] **Tianfu Xu** (ID),[1] **Hailong Tian** (ID),[1] **Guanhong Feng,**[1] **Zhijie Yang,**[1] **and Bing Zhou**[2]

[1]*Key Laboratory of Groundwater Resources and Environment, Ministry of Education, Jilin University, Changchun 130021, China*
[2]*Petroleum Exploration & Production Research Institute, SINOPEC, Beijing 100083, China*

Correspondence should be addressed to Hailong Tian; thl@jlu.edu.cn

To further understand the interactions of CO$_2$-brine-rock at geological time scales, in this study, a 1D reactive transport model of CO$_2$ intrusion into sandstone of the Longtan Formation (P$_2$l) in the Huangqiao area, China, was constructed based on site-specific data. The simulation time is consistent with the retention time of CO$_2$ in the Longtan sandstone Formation and is set to 20 Ma. The reactive transport model is calibrated and revised using the measured data for sandstone samples from Well X3 (i.e., the natural analogue). By comparing the simulation results with measured data for the natural analogue, the long-term geochemical reactions are investigated. The simulation results indicate that the brine-rock interactions induced by CO$_2$ can be roughly divided into two stages. First, susceptible minerals (e.g., chlorite, ankerite, calcite, and feldspar minerals) dissolve rapidly under acidic conditions formed by the dissolution of CO$_2$. The precipitation of siderite is facilitated by the dissolution of ankerite and chlorite. Smectite-Ca and dawsonite precipitate due to the dissolution of anorthite and albite, respectively. Dawsonite begins to convert into smectite-Na when albite is completely dissolved. As the reactions continue, intermediate products (i.e., illite, smectite-Na, and smectite-Ca) generated in the first stage become the reactants and subsequently react with CO$_2$ and brine. These three clay minerals are not stable under acidic conditions and transform into kaolinite and paragenetic quartz in the later stage of reaction. Comparing the simulation results of the Base Case with the measured data for the natural analogue and inspired by previous studies, the scour of kaolinite is supposed to have occurred in this region and is considered in the revised model by introducing a coefficient of the scour of kaolinite (i.e., Case 2). The simulation results of Case 2 fit well with the measured data on mineral assemblage, and the trend of the sandstone porosity growth caused by the CO$_2$-brine-rock reaction is captured by our simulation results. The combination of numerical simulation and natural analogue study indicates that the joint effects of long-term CO$_2$-brine-rock reactions and scour of kaolinite increase the pore space of the host rock and result in an increase in quartz content in the sandstone.

1. Introduction

Capturing carbon dioxide (CO$_2$) from the atmosphere and then injecting it into suitable geologic formations is considered an option to compensate for anthropogenic atmospheric emissions of CO$_2$ [1]. Such formations could include deep saline aquifers, depleted gas and oil reservoirs, and unmineable coal seams. For a long time, deep saline aquifers have appeared to be the most promising storage places for large quantities of CO$_2$ [2]. The wide global distribution of saline aquifers and their occurrence close to the potential CO$_2$

emission sources, such as coal-fired power plants, is particularly appealing [3]. The storage capacity of deep saline aquifers for CO$_2$ is very large and has been estimated to be as low as 320 Gt CO$_2$ [4] and as high as 200,000 Gt CO$_2$ [5].

Pure CO$_2$ is slightly reactive; however, once dissolved in brine, it forms H$_2$CO$_3$, which is a weak acid. This change causes a decrease in the pH of the brine and makes the brine reactive to the minerals it contacts. The impact of acidic fluids on rocks is illustrated by the damage from acid rain to historic buildings [6]. Generally, the solid skeleton of the saline aquifers consists of sandstone, with burial depths

between 800 and 2000 m. The salinity values vary between 100,000 (10% NaCl by weight) and 300,000 ppm (30% NaCl by weight) in most saline aquifers [7]. The interactions between saline aquifer pore fluid, CO_2, and rock create significant changes in the chemical and mineralogical structures of the aquifer formation [8] and affect the mechanical behavior of reservoir rock [9]. To assess the feasibility and security of current or future CO_2 storage projects, the mineral alteration and the evolution of rock physical properties induced by the injected CO_2 need to be investigated. Related studies have been conducted by experimental methods [10–13], numerical simulations [14–20], and natural analogues [21–24]. The short duration (several hours to several years) of the laboratory or field experiments, combined with the difficulty of observing mineral reactions and the sluggish nature of these reactions, results in a very limited observational database [25]. Therefore, numerical modeling is often employed for long-term CO_2 geological storage assessment, which can provide valuable insights into the chemical and physical consequences of CO_2 injection into the subsurface environment. However, such simulations rely on thermodynamic and kinetic databases that have uncertainty [26]. Consequently, the numerical simulation results of long-term CO_2-brine-rock interaction should be calibrated or validated by the natural accumulations of CO_2 (i.e., natural analogues) which have retained CO_2 for millions of years [27, 28].

Numerous natural CO_2 reservoirs have been found in the world, and some of them have been used as analogues to provide natural evidence for evaluating the impacts of CO_2 geological storage over long time scales [29–34]. Ren et al. [35] reported that the Huangqiao CO_2 field in eastern China is unique with the coexistence of CO_2 and hydrocarbon accumulations and that the CO_2-rich fluid induced substantial reformation of the Longtan sandstone reservoir. The core test results show that carbonate and feldspar minerals are completely dissolved in the sandstone and that the main component of the rock is quartz with small amounts of clay minerals (detailed in Section 3). These authors conducted a set of CO_2-brine-sandstone interaction experiments from 60°C to 120°C and from 10 MPa to 40 MPa, which correspond to burial depths from 1500 m to 4000 m, to understand the corrosion of CO_2-rich fluid on the sandstone reservoir. Experimental results indicated that the corroded mineral is mainly carbonate and that the corrosion reached equilibrium after 72 h. The corrosion of feldspar was not detected by Ren et al. [35] because aluminosilicate mineral alteration is very slow under ambient deep-aquifer conditions and is not amenable to an experimental study lasting a few days [36]. To date, how the sandstone in the Huangqiao CO_2 reservoir became quartzose and what were the major reactions among the CO_2, brine, and sandstone are still unknown.

To further understand the long-term interaction among the dissolved CO_2, brine, and sandstone and the impact of the reactions on the physical and mineralogical characteristics of the strata, in this paper, the natural CO_2 reservoir in the Huangqiao area, Southeast China, is selected as the natural analogue for long-term CO_2-brine-rock interactions. A one-dimensional geochemical reactive transport model is constructed to reproduce the brine-rock reactions induced

by CO_2 over long time scales. The simulation results are calibrated by the observations in the Huangqiao natural CO_2 reservoir.

2. Geological Background

The research area, the Huangqiao CO_2 reservoir, is located in Huangqiao Township, Jiangsu Province, Southeast China, and has been commercially exploited for more than 35 years since 1983. The Huangqiao region is in the southern North Jiangsu Basin. Its tectonic structure is the Huangqiao complex syncline in the northeastern Nanjing Depression (Figure 1(a)).

The Huangqiao region is widely covered by Quaternary deposits. All other strata are basically well preserved, except for Paleogene, Lower Cretaceous, Jurassic, and Upper Triassic strata (detailed stratigraphic information is shown in Figure 2). As presented in Figure 2, eight CO_2 reservoirs have been detected in this area with a proven CO_2 reserve of 196.9×10^8 m^3 [38]. The origin of CO_2 has been inferred to be the mantle or magma in previous studies [38, 39], and the deep faults are the main channels for CO_2 migration to shallow strata. Cui [40] suggested that the CO_2 confined in the deeper strata of P_1q migrated upward along the fault (as shown in Figure 1(b)) to the Permian Longtan Formation (P_2l), the target strata of our study, in the Neogene period (approximately 20 Ma) because of tectonic movement. The overlying strata (P_2d) consisting of ~50 m thick mudstone with siltstone layers inhibit the upward migration of CO_2 due to their low permeability and high capillary entry pressure [41]. Consequently, a large amount of CO_2 has accumulated in the Longtan Formation to form the CO_2 reservoir there. The Longtan Formation is an ~140 m thick unit of interbedded black mudstone and grey-black sandstone, with thin coal interlayers. The sandstone is the main CO_2-producing section in Well X3 [38]. According to the local burial history (Figure 3), P_2l has undergone slight subsidence since the Neogene Period, and the burial depth of P_2l in this period is approximately 1600 m with a temperature of approximately 70°C.

3. Core Mineralogy Test Data Analysis

Several wells were drilled in this region for the exploration or exploitation of oil and CO_2 (the distribution of the drillings can be found in Figure 1b in [38]), most of which were drilled through or into the P_2l sandstone formation and P_2l was sampled. The mineral compositions of the core samples were obtained through X-ray diffraction (XRD) and thin section analysis, which were carried out by the East China branch of SINOPEC. The testing procedures and methods are not the focus of our study and are not discussed here. To meet the format of the simulation code TOUGHREACT (detailed in the next section) for defining mineral abundance, the mass fractions of minerals directly measured by XRD analysis were converted to volume fractions.

A total of 18 core samples of P_2l sandstone formation from three wells (i.e., Wells X1, X2, and X3) were tested, and the sampling depth and mineral composition of each sample are listed in Table 1. The lithology of core samples
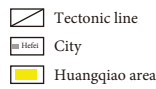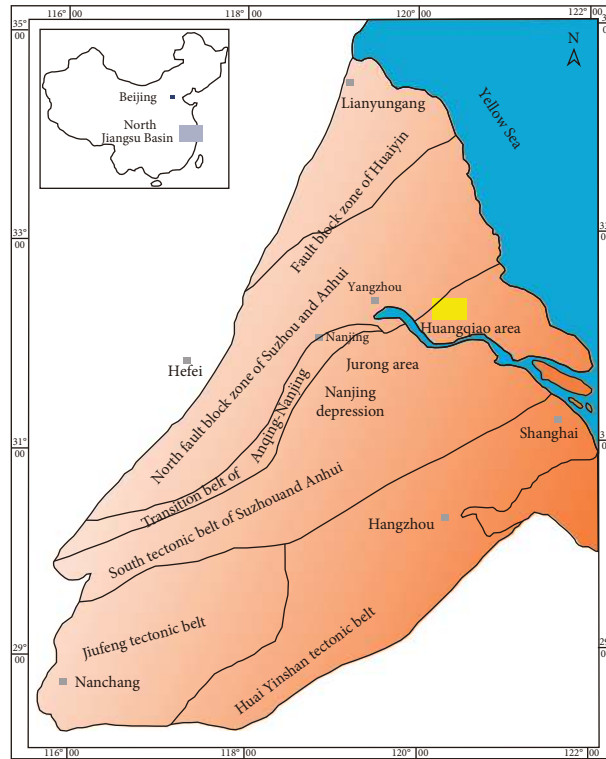
(a)
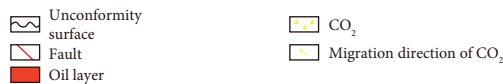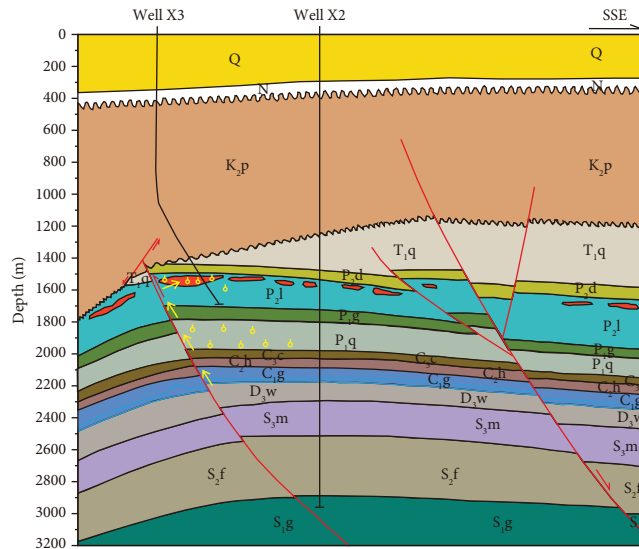
(b)

FIGURE 1: Tectonic units of the Lower Yangtze region and Huangqiao area (a) (modified from Ge and Zhang [37]). Simplified geological section of Well X1 and X3 (b) (from Ren et al. [35]). The meanings of the stratigraphic symbols and the lithology of the strata can be found in Figure 2.

Erathem	Series	Formation	Depth (m)	Lithology	Description
Cenozoic	Quaternary	Dongtai (Qd)			Variegated clay, gravel interlayers
	Tertiary	Yancheng (Ny)			Grey green and brown clay layers, interbedded grey white gravel layers
Mesozoic	Cretaceous	Pukou (K₂p)	500 1000		Brown-dark brown mudstone, sandy mudstone sandstone with sandstone interlayers; the bottom is mainly conglomerate bottom. containing gypsum and gas
	Triassic	Qinglong (T₁q)			Dark grey limestone, with mudstone and dolomitic mudstone interlayers
Paleozoic	Permian	Dalong (P₂d)			Dark grey-grey black dolomite mudstone, with thin grey siltstone interlayers
		Longtan (P₂l)	1500		Grey-black sandstone interbedded black mudstone, with thin coal interlayers
		Gufeng (P₁g)			Grey black dolomite mudstone with sandstone interlayers
		Qixia (P₁q)	2000		Grey black limestone with chert
	Carboniferous	Chuanshan (C₃c)			Grey limestone with thin mudstone interlayers
		Huanglong (C₂h)			Light grey limestone
		Gaolishan (C₁g)			Variegated mudstone and sandstone are interbeded, with dark grey sandstone and mudstone in the bottom
	Devonian	Wutong (D₃w)	2500		Grey white quartz sandstone
	Silurian	Maoshan (S₃m)			Purplish red sandstone and mudstone
		Fentou (S₂f)			Grey-dark grey sandstone and mudstone are interbedded
		Gaojiabian (S₁g)			Dark black mudstone

Legend:
- Clay
- Conglomerate
- Siltstone
- Limestone
- Sandstone
- Gypsum
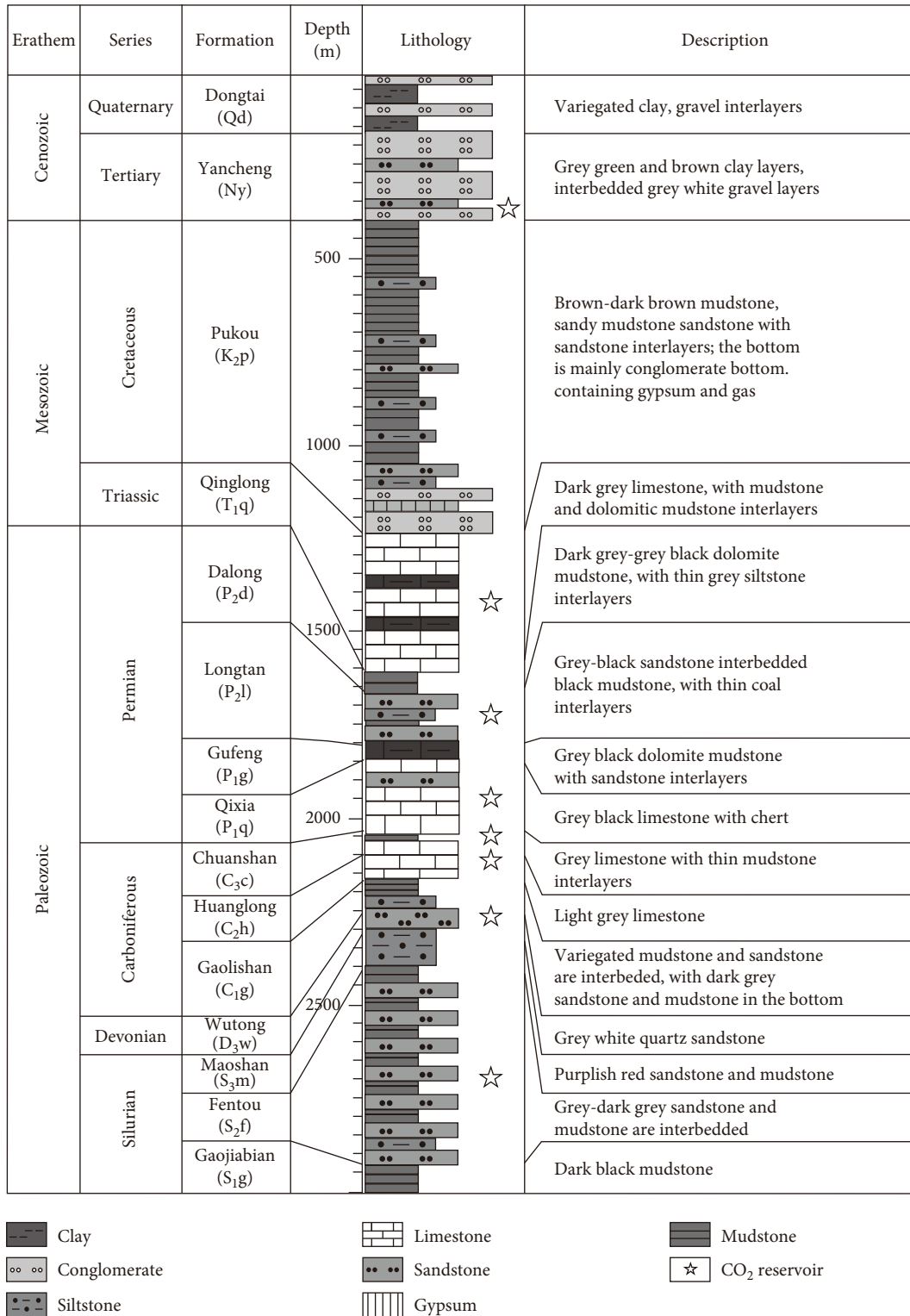- Mudstone
- ☆ CO_2 reservoir

Figure 2: Stratigraphic column of the Huangqiao area (from Liu et al. [38]).

from Well X1 is fine- to medium-grained feldspathic quartzose sandstone, with quartz contents (in volume fraction) of 41.4% to 66%. Illite is the main clay mineral, with the content ranging from 14.7% to 22.2%. Feldspar minerals are dominated by plagioclase with contents of 3.1% to 16%. K-feldspar and carbonate minerals (e.g., calcite, ankerite, and siderite) are found in a portion of the samples from Well X1, with contents ranging from a few percent to more than a dozen percent. Similar to the samples from Well X1, the mineral composition of samples taken from Well X2 is
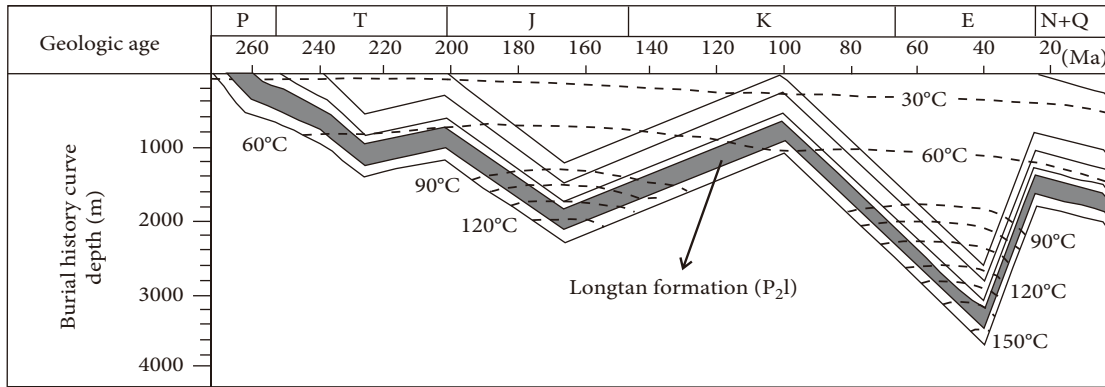
FIGURE 3: The burial history curve of the Longtan Formation (P_2l) in the Huangqiao area (from Sy [42]).

TABLE 1: Volume fractions of minerals in sandstone samples taken from the Longtan Formation (converted from XRD analysis data).

Number	Well	Depth (m)	Quartz (%)	Illite (%)	Kaolinite (%)	Chlorite (%)	Smectite (%)	Plagioclase (%)	K-feldspar (%)	Calcite (%)	Ankerite (%)	Siderite (%)	Barite (%)
X1-1	X1	1868.1	66.0	20.2	0.0	0.2	1.9	5.3	0	2.7	0	0	3.7
X1-2	X1	1877.5	57.8	19.5	0.0	0.9	1.8	13.7	0	2.7	0	0	3.6
X1-3	X1	1878.52	52.1	14.7	0.0	1.2	1.3	12.9	0	1.2	0	12.2	4.4
X1-4	X1	1970	48.0	22.2	1.4	3.0	0.7	9.1	0	5.7	0	5.7	4.2
X1-5	X1	1995	41.4	21.3	1.3	4.0	1.8	3.1	2.2	0	8.2	9.8	6.9
X1-6	X1	2056	48.5	14.8	0.7	1.8	0.5	16	2.3	6.5	1.7	4.2	3
X2-1	X2	1548.02	69.3	8.1	0.0	0.4	0.7	11.7	0	0	0	5.5	4.3
X2-2	X2	1552.53	52.8	19.4	0.0	0.4	1.1	13	0	3	0	6.5	3.8
X2-3	X2	1553.86	44.4	34.0	0.0	1.7	6.4	6.7	0	0	0	3.5	3.3
X2-4	X2	1557.15	50.4	28.0	0.0	0.0	2.1	11.6	0	1.7	0	3.1	3.1
X2-5	X2	1559.14	56.3	23.8	0.0	1.6	0.9	12.2	0	1.8	0	0	3.4
X2-6	X2	1629.68	62.5	9.8	0.0	1.7	0.8	19.1	0	2.5	0	0	3.6
X2-7	X2	1631.73	52.6	10.4	0.0	1.8	1.0	14.2	0	8.3	0	5.2	6.5
X2-8	X2	1636.75	69.3	7.3	0.0	1.7	0.3	11.7	0	0	0	5.5	4.2
X3-1	X3	1595	85.7	5.0	2.8	0.0	0.3	0	0	0	0	0	6.2
X3-2	X3	1597.1	88.6	2.2	1.7	0.0	0.1	0	0	0	0	0	7.4
X3-3	X3	1598.3	86.9	3.2	2.8	0.0	0.2	0	0	0	0	0	6.9
X3-4	X3	1598.5	89.1	3.2	2.3	0.0	0.2	0	0	0	0	0	5.2

dominated by quartz (44.4%-69.3%), illite (7.3%-34%), and plagioclase (6.7%-19.1%). Kaolinite, K-feldspar, and ankerite are not detected in the samples from Well X2. Calcite and siderite are detected in most of the samples from Well X2, with abundances of several percent. Four samples from Well X3 were tested, and the testing results indicate that the lithology of the formation is medium-grained quartzose sandstone with extremely high contents of quartz (85.7%-89.1%). The contents of clay minerals of samples from Well X3, with volume fractions of 4% to 8%, are relatively low compared to those of samples taken from Wells X1 and X2. In addition, the abundance of kaolinite in samples from Well X3 is significantly higher than those in samples taken from Wells X1 and X2, and chlorite that is commonly found in Wells X1 and X2 is not detected in Well X3. Plagioclase, calcite, and siderite, which are common in samples from Wells X1 and X2, are

not found in those from Well X3. K-feldspar and ankerite are not detected in samples from Well X3.

As shown in Figure 1(b), Well X3 is located northwest of Well X2 at a distance of ~1 km. Well X1 is located approximately 4 km southeast of Well X2 (as presented in Figure 1b in [38]). In other words, the three wells are not far apart, so why are the mineral compositions of samples from Well X3 so different from those of samples from Wells X1 and X2? It should be noted that CO_2 is yielded only in Well X3 in the Longtan sandstone Formation and no CO_2 is found in the same strata in Wells X1 and X2. Ren et al. [35] proposed that the existence of CO_2-induced brine-rock interactions in Well X3 is the main reason for the differences between the sandstone reservoirs of Well X3 and Well X2. However, due to the limited duration (120 h) of their experiments, only carbonate minerals were found to be eroded,

which could not explain why the sandstone samples from Well X3 do not contain feldspar minerals and why only quartz and a small amount of clay minerals are detected. Therefore, we intend to use a combination of numerical simulation and natural analogy to explore whether the brine-rock interactions induced by CO_2 resulted in such large differences in the core sample mineral compositions between Well X3 and Wells X1 and X2. If so, what are the main geochemical reactions, and how long do they take?

4. Numerical Modeling Approach

All present simulations were carried out using the nonisothermal, reactive transport modeling code TOUGHREACT [43], which has been widely used for CO_2 geological sequestration [44–46]. This code was developed by introducing reactive transport into the existing framework of a nonisothermal multiphase multicomponent fluid and heat flow simulator TOUGH2 [47]. Complicated thermophysical-chemical processes are considered under various thermohydrological and geochemical conditions of pressure, temperature, ionic strength, and water saturation. TOUGHREACT can be applied to one-, two-, or three- dimensional porous and fractured media with physical and chemical heterogeneity. The code can accommodate any number of chemical species present in liquid, gas, and solid phases. Further descriptions about the selection of the kinetic and thermodynamic parameters are provided in Appendix A.

5. Model Setup

5.1. Conceptual Model and Boundary Conditions. As shown in Figure 1(b), due to the sealing effect of the overlying P_2d mudstone strata, CO_2 transported upward along the fault migrated laterally and accumulated in the Longtan sandstone Formation. Well X3 is located in this CO_2 reservoir, and the sandstone samples taken from the well are presumed to have been eroded by the CO_2-rich flow. To simulate the effect of long-term CO_2-brine-sandstone interaction on the physical properties (e.g., porosity) and mineral composition of the sandstone reservoirs, much specific and detailed information is required, e.g., the thickness and lateral extension of the sandstone strata, the physical properties and mineral composition of the sandstone, and its spatial heterogeneity. Before moving into the all-encompassing investigation, general features and issues related to these processes need to be explored. This exploration can be done by investigating a one-dimensional CO_2 source-sandstone system that abstracts the site-specific features and is able to represent characteristics that are common to many such systems.

As presented in Figure 4, a one-dimensional horizontal column is used to represent the CO_2 source-sandstone system in the model. Considering the extremely long modeling period (20 Ma), only three grids with different roles are set in the model to reduce the CPU load. The grid on the left is set as the source of the CO_2, and an overpressure of 0.5 MPa is assigned to it to ensure the CO_2 flow into the sandstone formation that is represented by the grid in the middle.
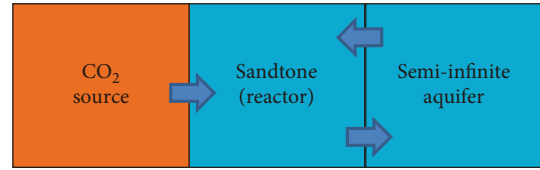

FIGURE 4: One-dimensional conceptual model of CO_2 intrusion into the Longtan sandstone Formation.

The size of the middle grid is set to 5 m × 5 m × 5 m to represent the sandstone formation that was invaded by CO_2 as revealed by Well X3. The pressure of the left grid is assumed to be constant throughout the simulation (i.e., it represents a Dirichlet boundary), which implies that the CO_2 consumed by the reactions will always be replenished. The geochemical reactions stop once the native water is drained by CO_2. To ensure that the CO_2-brine-rock interactions continue in the simulation, a water- (brine) saturated grid with infinite volume is set in the right to represent the lateral semi-infinite aquifer.

5.2. Initial Conditions. The geochemical simulation should begin as the CO_2 invades the Longtan sandstone Formation, and the initial conditions in our model should correspond to the conditions at this moment. As mentioned above, the CO_2 invaded the target sandstone strata in the Neogene Period (approximately 20 Ma) along the fracture. Therefore, it is a major challenge to obtain the initial physical parameters and mineralogical composition of the host rock and the initial native water components, because all the measured physical and mineral data are the present-day observations.

As mentioned in Section 3, CO_2 is observed only in Well X3 in the target strata, and the sandstone samples taken from the same formation from adjacent Wells X1 and X2 are presumed not to have been eroded by CO_2. Moreover, the burial depth of the P_2l formation after the Neogene Period changed little, and its temperature and pressure conditions were relatively stable (see Figure 3). Therefore, as previously assumed by Watson et al. [33], the mineralogy and physical properties of the sandstone formation outside the CO_2 reservoir (i.e., Wells X1 and X2) are taken as unmodified and can be approximated as the initial conditions for the sandstone formation in Well X3.

5.2.1. Initial Physical Parameters. Most hydrogeological and physical parameters (i.e., porosity, permeability, and density) of the sandstone in our model are set to the average values from test results of the samples from Wells X1 and X2 (listed in Table 2). The burial depth of P_2l is approximately 1600 m after the Neogene Period, and the ambient temperature is approximately 70°C (see Figure 3). Therefore, the initial temperature is set to 70°C and is assumed to be constant over time. In addition, the initial pore water pressure of the strata is set to 16 MPa by hydrostatic equilibrium. As stated before, an overpressure of 0.5 MPa is set in the left grid, and the pressures of left and right grids are set to be constant throughout the simulation. The relative

TABLE 2: Physical parameters for the Longtan sandstone Formation.

Rock properties	
Porosity (%)	6.52
Permeability (10^{-15} m^2)	0.68
Density (kg·m^{-3})	2.53
Temperature (°C)	70
Pressure (MPa)	16/16.5
Relative permeability parameters (van Genuchten model)	
$m = 1 - 1/n$	0.42
Residual liquid saturation	0.15
Liquid saturation	1.0
Residual gas saturation	0.01
Capillary pressure parameters (van Genuchten model)	
$m = 1 - 1/n$	0.42
Residual liquid saturation	0.15
$1/P_0$ (Pa^{-1})	1.00e-6
Pmax (Pa)	1.00e6
Liquid saturation	1.0

permeability and capillary pressure parameters are set empirically to represent the properties of sandstone in the Huangqiao area and are listed in Table 2.

5.2.2. Initial Conditions for Geochemistry. The initial conditions for geochemistry include the initial mineral composition and water chemistry. The average mineral composition of samples taken from Wells X1 and X2 is set as the initial mineral assemblage for sandstone in our model. Plagioclase is treated as a 1 : 1 mixture of endmembers albite and anorthite in the model to simplify the mineralogy [48, 49]. Similarly, smectite is treated as a 1 : 1 mixture of smectite-Na and smectite-Ca (detailed in Table 3). The measured native formation water chemical composition, taken from Ren et al. [35], is used during the initialization of the simulations. The resulting water composition is used as the initial condition for the subsequent modeling (Table 4).

6. Results and Discussion

6.1. Mineral Alternation. We started the first simulation using the parameters given in Tables 2–4 (called the Base Case simulation). The flooding of CO_2 decreases the pH of the solution and makes it acidic which induces the dissolution of some minerals. To understand the long-term mineral alteration pattern in sandstone, the variations in the mineral abundances (expressed in the volume fraction of mineral in the medium) are presented in Figure 5. As shown in the figure, feldspar minerals including anorthite and albite (Figure 5(a)) and K-feldspar (Figure 5(b)) dissolve significantly and disappear after approximately 8000 years, 22,000 years, and 100,000 years, respectively. For clay minerals, chlorite (Figure 5(c)) is the most reactive under acidic conditions formed by the dissolution of CO_2 and dissolves completely after 8000 years. Illite (Figure 5(d)) precipitates slightly between 300 and 10,000

TABLE 3: Initial mineral volume fractions in the sandstone and possible secondary mineral phases in the simulation.

Mineral	Chemical formula	Volume fraction (%)
Primary		
Quartz	SiO_2	55.11
Illite	$K_{0.6}Mg_{0.25}Al_{1.8}(Si_{3.5}Al_{0.5}O_{10})(OH)_2$	18.02
Kaolinite	$Al_2Si_2O_5(OH)_4$	0.39
Chlorite	$Mg_{2.5}Fe_{2.5}Al_2Si_3O_{10}(OH)_8$	1.45
Smectite-Na	$Na_{0.29}Mg_{0.26}Al_{1.77}Si_{3.97}O_{10}(OH)_2$	0.725
Smectite-Ca	$Ca_{0.145}Mg_{0.26}Al_{1.77}Si_{3.97}O_{10}(OH)_2$	0.725
Albite	$NaAlSi_3O_8$	5.725
Anorthite	$CaAl_2Si_2O_8$	5.725
K-feldspar	$KAlSi_3O_8$	0.32
Calcite	$CaCO_3$	2.58
Ankerite	$CaMg_{0.3}Fe_{0.7}(CO_3)_2$	0.71
Siderite	$FeCO_3$	4.37
Barite	$BaSO_4$	4.15
Secondary		
Dawsonite	$NaAlCO_3(OH)_2$	
Dolomite	$CaMg(CO_3)_2$	
Magnesite	$MgCO_3$	

TABLE 4: Initial total dissolved component concentrations in the water for reactive transport simulation.

Component	Concentration (mol/kg H_2O)
Ca	0.299×10^{-3}
Mg	0.435×10^{-4}
Na	0.310
K	0.606×10^{-5}
Fe	0.263×10^{-5}
Al	0.281×10^{-7}
Si	0.752×10^{-3}
C	0.779×10^{-1}
S	0.714×10^{-2}
Cl	0.229
pH	6.84

years. Then, it begins to dissolve and disappears after approximately 1.2 Ma. K^+ to form illite is provided by the dissolution of K-feldspar. The carbonate mineral siderite (Figure 5(e)) precipitates slightly at the expense of chlorite and then begins to dissolve. The dissolution of ankerite (Figure 5(e)) also provides Fe^{2+} for the precipitation of siderite. Calcite (Figure 5(e)) dissolves rapidly under high CO_2 pressure conditions and disappears after approximately 70 years. As a secondary mineral (does not exist initially), dawsonite (Figure 5(e)) is generated after approximately 30 years and precipitates significantly with a maximum abundance of 4.6% after 80,000 years. The
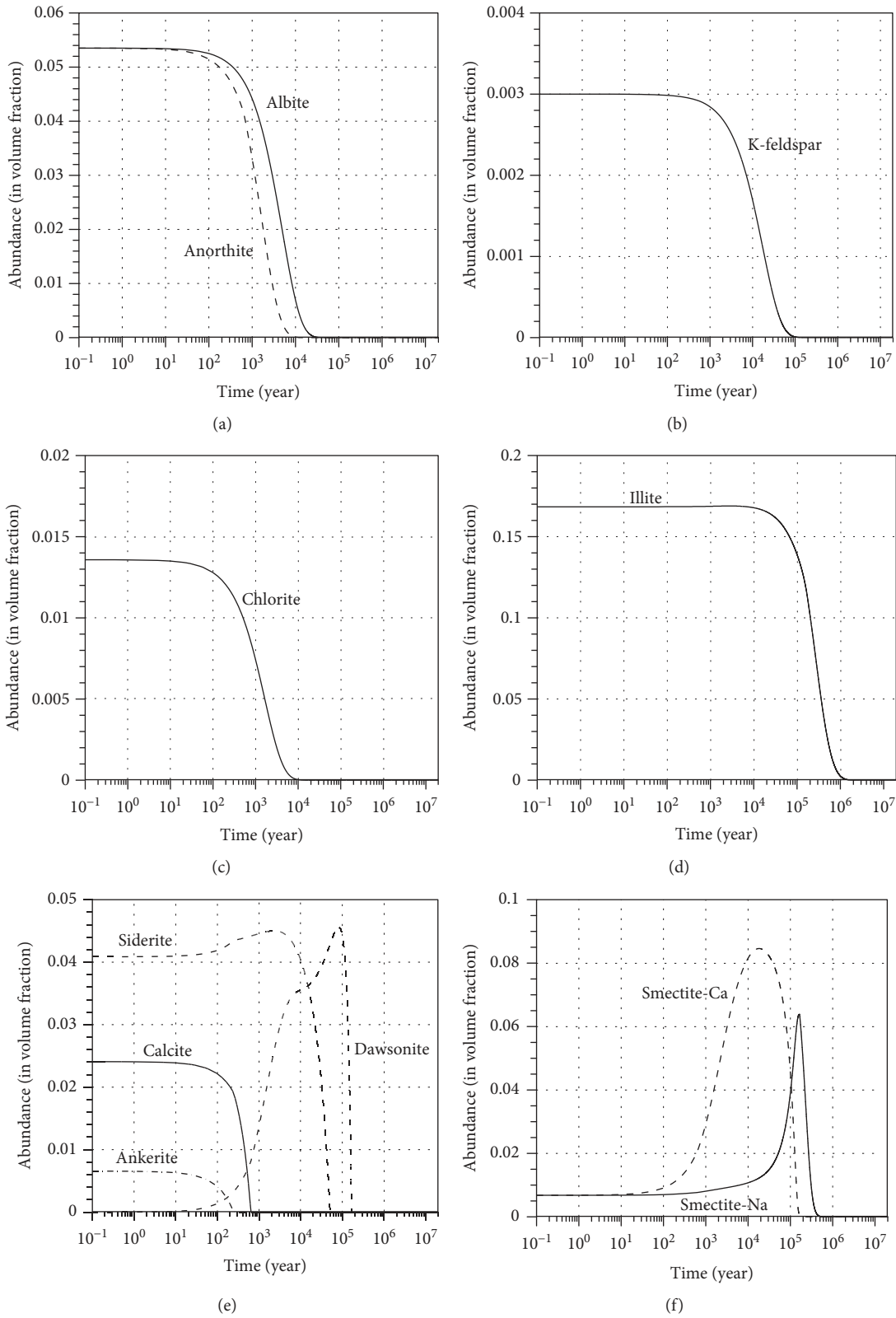
(a)

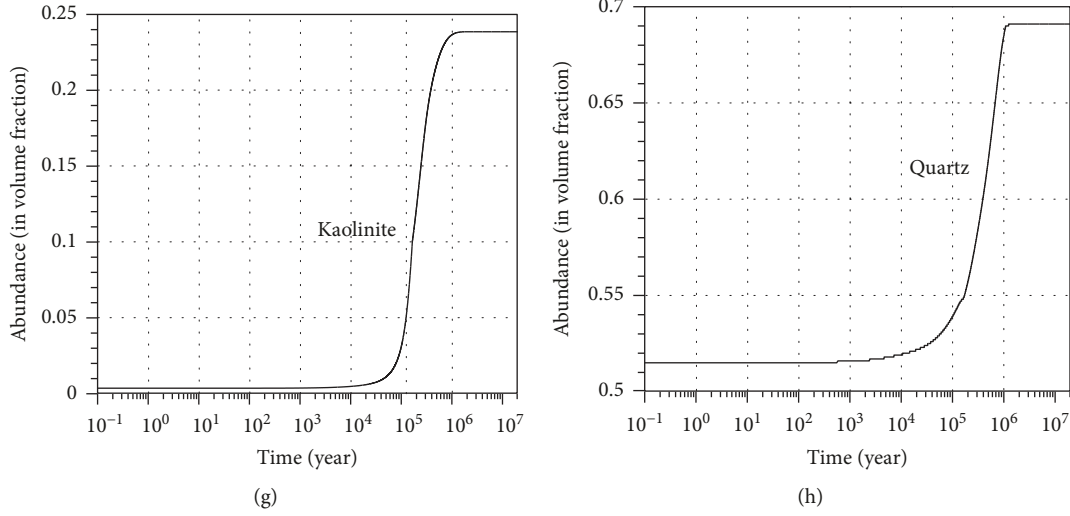(b)

(c)

(d)

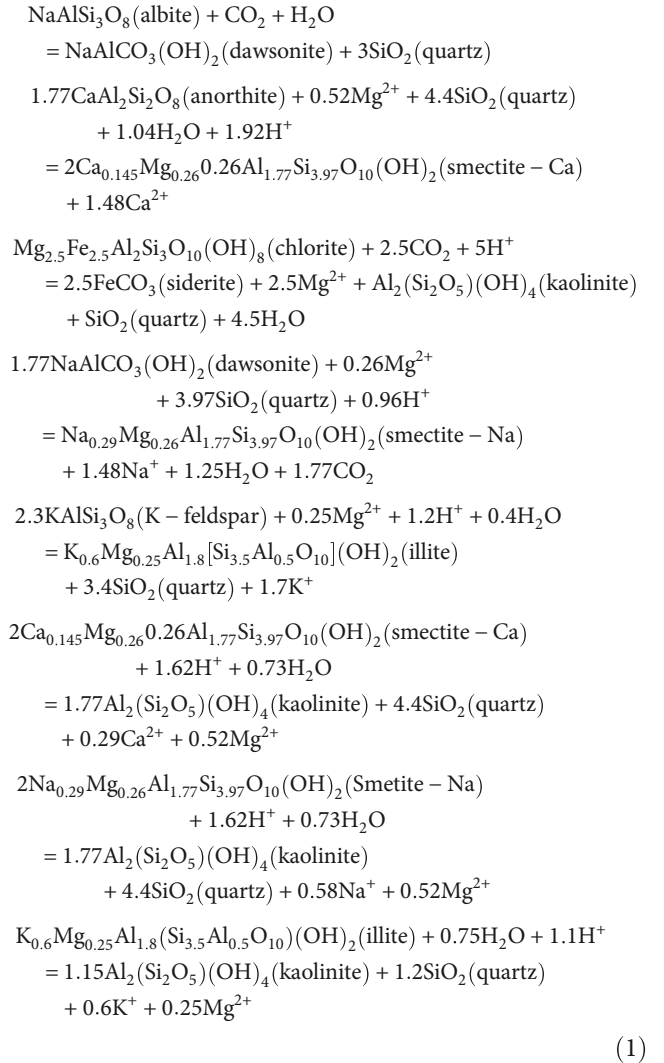(e)

(f)

Figure 5: Continued.

(g)

(h)

FIGURE 5: Variations in abundance (in volume fraction of medium) of albite and anorthite (a); K-feldspar (b); chlorite (c); illite (d); calcite, siderite, ankerite, and dawsonite (e); smectite-Na and smectite-Ca (f); kaolinite (g); and quartz (h) after flooding by CO_2.

formation of dawsonite is facilitated by the dissolution of albite. After 80,000 years, when albite has dissolved completely, the dawsonite begins to dissolve and disappears after approximately 170,000 years. The dissolution of dawsonite provides Na^+ for the precipitation of smectite-Na (Figure 5(f)). In addition, Ca^{2+} needed for the formation of smectite-Ca (Figure 5(f)) is derived from the dissolution of anorthite and calcite. The simulation results indicate that illite, smectite-Na, and smectite-Ca are unstable under acidic conditions and eventually convert to kaolinite and paragenetic quartz. Consequently, kaolinite (Figure 5(g)) and quartz (Figure 5(h)) precipitate significantly throughout the simulation period and become the dominant minerals at the end of the simulation.

The CO_2-brine-rock geochemical reaction processes can be roughly divided into two stages. Major reactants in the first stage (probably the first 10,000 to 100,000 years of the simulation) include calcite, ankerite, chlorite, and feldspar minerals. Carbonate minerals siderite and dawsonite and clay minerals smectite-Na, smectite-Ca, and illite are products of reactions in the first stage and become reactants to react with CO_2 and water in the second stage when the first reactants (i.e., chlorite and feldspars) have completely dissolved. The precipitation of carbonate minerals could immobilize CO_2 (i.e., mineral trapping). Our simulation results indicate that carbonate minerals may dissolve as the reaction continues. However, on the time scale that may be concerned in the CO_2 geologic storage project, i.e., 5,000 to 10,000 years, the carbonate minerals (e.g., siderite and dawsonite) precipitate significantly. It should be noted that illite, which is usually supposed to be stable under neutral or alkaline conditions [50, 51], becomes the main reactant in the second stage of the reaction. Our simulation results indicate that illite could convert to kaolinite in the acidic environment formed by CO_2. The main products in the second stage are quartz and kaolinite, which are stable under acidic conditions. Finally, the mineralogy of sandstone is dominated by quartz and kaolinite, with volume fractions of 69.1%

and 23.9%, respectively. The main CO_2-related reactions mentioned above are summarized as follows:

$$
\begin{aligned}
&NaAlSi_3O_8\,(albite) + CO_2 + H_2O \\
&\quad = NaAlCO_3(OH)_2\,(dawsonite) + 3SiO_2\,(quartz)
\end{aligned}
$$

$$
\begin{aligned}
&1.77CaAl_2Si_2O_8\,(anorthite) + 0.52Mg^{2+} + 4.4SiO_2\,(quartz) \\
&\quad + 1.04H_2O + 1.92H^+ \\
&= 2Ca_{0.145}Mg_{0.26}0.26Al_{1.77}Si_{3.97}O_{10}(OH)_2\,(smectite - Ca) \\
&\quad + 1.48Ca^{2+}
\end{aligned}
$$

$$
\begin{aligned}
&Mg_{2.5}Fe_{2.5}Al_2Si_3O_{10}(OH)_8\,(chlorite) + 2.5CO_2 + 5H^+ \\
&= 2.5FeCO_3\,(siderite) + 2.5Mg^{2+} + Al_2(Si_2O_5)(OH)_4\,(kaolinite) \\
&\quad + SiO_2\,(quartz) + 4.5H_2O
\end{aligned}
$$

$$
\begin{aligned}
&1.77NaAlCO_3(OH)_2\,(dawsonite) + 0.26Mg^{2+} \\
&\qquad\quad + 3.97SiO_2\,(quartz) + 0.96H^+ \\
&= Na_{0.29}Mg_{0.26}Al_{1.77}Si_{3.97}O_{10}(OH)_2\,(smectite - Na) \\
&\quad + 1.48Na^+ + 1.25H_2O + 1.77CO_2
\end{aligned}
$$

$$
\begin{aligned}
&2.3KAlSi_3O_8\,(K - feldspar) + 0.25Mg^{2+} + 1.2H^+ + 0.4H_2O \\
&= K_{0.6}Mg_{0.25}Al_{1.8}[Si_{3.5}Al_{0.5}O_{10}](OH)_2\,(illite) \\
&\quad + 3.4SiO_2\,(quartz) + 1.7K^+
\end{aligned}
$$

$$
\begin{aligned}
&2Ca_{0.145}Mg_{0.26}0.26Al_{1.77}Si_{3.97}O_{10}(OH)_2\,(smectite - Ca) \\
&\qquad\quad + 1.62H^+ + 0.73H_2O \\
&= 1.77Al_2(Si_2O_5)(OH)_4\,(kaolinite) + 4.4SiO_2\,(quartz) \\
&\quad + 0.29Ca^{2+} + 0.52Mg^{2+}
\end{aligned}
$$

$$
\begin{aligned}
&2Na_{0.29}Mg_{0.26}Al_{1.77}Si_{3.97}O_{10}(OH)_2\,(Smetite - Na) \\
&\qquad\quad + 1.62H^+ + 0.73H_2O \\
&= 1.77Al_2(Si_2O_5)(OH)_4\,(kaolinite) \\
&\quad + 4.4SiO_2\,(quartz) + 0.58Na^+ + 0.52Mg^{2+}
\end{aligned}
$$

$$
\begin{aligned}
&K_{0.6}Mg_{0.25}Al_{1.8}(Si_{3.5}Al_{0.5}O_{10})(OH)_2\,(illite) + 0.75H_2O + 1.1H^+ \\
&= 1.15Al_2(Si_2O_5)(OH)_4\,(kaolinite) + 1.2SiO_2\,(quartz) \\
&\quad + 0.6K^+ + 0.25Mg^{2+}
\end{aligned}
$$

$$\text{(1)}$$

6.2. Porosity Changes. Potential mineral dissolution and precipitation may affect the porosity of the sandstone. Variation in sandstone porosity is simulated in our model and illustrated in Figure 6. The variation in porosity is calculated using changes in the volume fraction of minerals as follows [43]:

$$\varnothing = 1 - \sum_{m=1}^{nm} fr_m - fr_\mu, \quad (2)$$

where $\varnothing$ is the porosity, superscript nm is the number of the minerals, fr_m is the volume fraction of mineral m in the rock, and fr_μ is the volume fraction of the inactive portion in the rock.

As shown in Figure 6, three peaks appear on the porosity curve over time. The first peak appears after 700 years, which is caused by the significant dissolution of calcite, ankerite, albite, and anorthite. After this time, when calcite is completely dissolved, the porosity of sandstone decreases to a certain extent due to the precipitation of smectite-Ca, dawsonite, and siderite. After approximately 3000 years, the variation in sandstone porosity is dominated by the dissolution of siderite, illite, and feldspar minerals, which results in an increase in porosity. The second wave crest of the porosity curve arises after approximately 50,000 years. Then, the porosity of rock decreases between 50,000 and 100,000 years, dominated by the precipitation of smectite-Na and dawsonite. After 100,000 years, the dissolution of dawsonite and smectite-Na results in an increase in sandstone porosity and the third peak of porosity curve appears after 200,000 years with a value of 13.2%. After this point, the geochemical reactions in the system are dominated by the conversion of smectite-Na and illite to kaolinite and paragenetic quartz. The joint effects of these two reactions reduce the pore space of the host rock, and the porosity of the rock decreases to 3.12% after 1 Ma. The simulation results indicate that the geochemical reaction reaches dynamic equilibrium after 1 Ma and that the mineral contents and rock porosity no longer change.

6.3. Comparison with the Natural CO_2 Reservoir. A comparison between modeling results and field observations of the natural CO_2 reservoir is instructive, because it helps identify issues and limitations in the models and places where the models need to be improved.

The observed mineral compositions of the natural CO_2 sandstone reservoir in the Huangqiao area are listed in Table 1 (i.e., core samples from Well X3) and are characterized by the extremely high abundance of quartz (>85%), small amounts of clay minerals (4-8.1%), and the absence of chlorite, carbonate, and feldspar minerals. The simulated mineral composition in the late stage of reaction in the Base Case shows good agreement with field data, including the absence of chlorite, carbonate, and feldspar minerals; significant dissolution of illite; and overgrowth of quartz. However, the simulated abundance of kaolinite is extremely high (>20%), which is inconsistent with the measured data. In addition, the simulated porosity of sandstone, i.e., 3.12% at
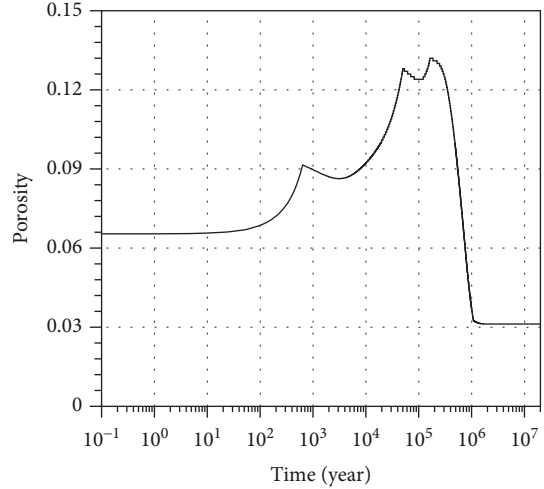

FIGURE 6: Variation of simulated porosity of sandstone versus time in the Base Case.

the end of the simulation, is much lower than the average value of measured data (15%). The contradictions between modeling results and the measured data in the mineral abundances (mainly in kaolinite content) and rock porosity indicate that there are still some shortcomings in our models. The best knowledge and efforts should be used to eliminate these shortcomings.

Higgs et al. [24] analyzed the sandstone cores from a high CO_2 concentration well (Garvoc-1) in the Otway Basin, Australia, and found that kaolinite is the dominant authigenic clay mineral with the bulk fraction distributed between 1.8% and 22.2% (the largest value of kaolinite bulk fraction is very close to our simulation result). They also found that the authigenic kaolinite occurred as very fine, grain-coating clays that may tend to be washed away by fluid flow. The loose sand grains (quartz) that are very common in the Garvoc-1 cuttings suggest that the fine kaolinite has been washed away. This process can explain why the abundance of kaolinite in sandstone cores from the same well is unevenly distributed, with the lowest value of 1.8% and the largest value of 22.2%. Cao et al. [52] found that the authigenic kaolinite in the sand reservoir migrates away instead of precipitating in situ in a strong flow system. The sandstone cores in Well X3 in the Huangqiao area contain loose quartz grains and have developed a large number of granules and intergranular pores [35]. Moreover, kaolinite was identified as the main fine mineral associated with fine migration-related formation damage in previous studies [53–56]. Considering the above evidence, we propose that a portion of authigenic kaolinite has been washed away in the Longtan sandstone Formation under the strong flow system caused by the intrusion of CO_2, which can explain why the simulated abundance of kaolinite in the Base Case is much higher than the observations from cores. As the scour and formation of kaolinite occur simultaneously, the process of kaolinite washing away must be coupled in reactive transport modeling.

The invoked simulation program TOUGHREACT (ECO2N module) does not consider minerals as fluid components. To describe the erosion process of kaolinite, the
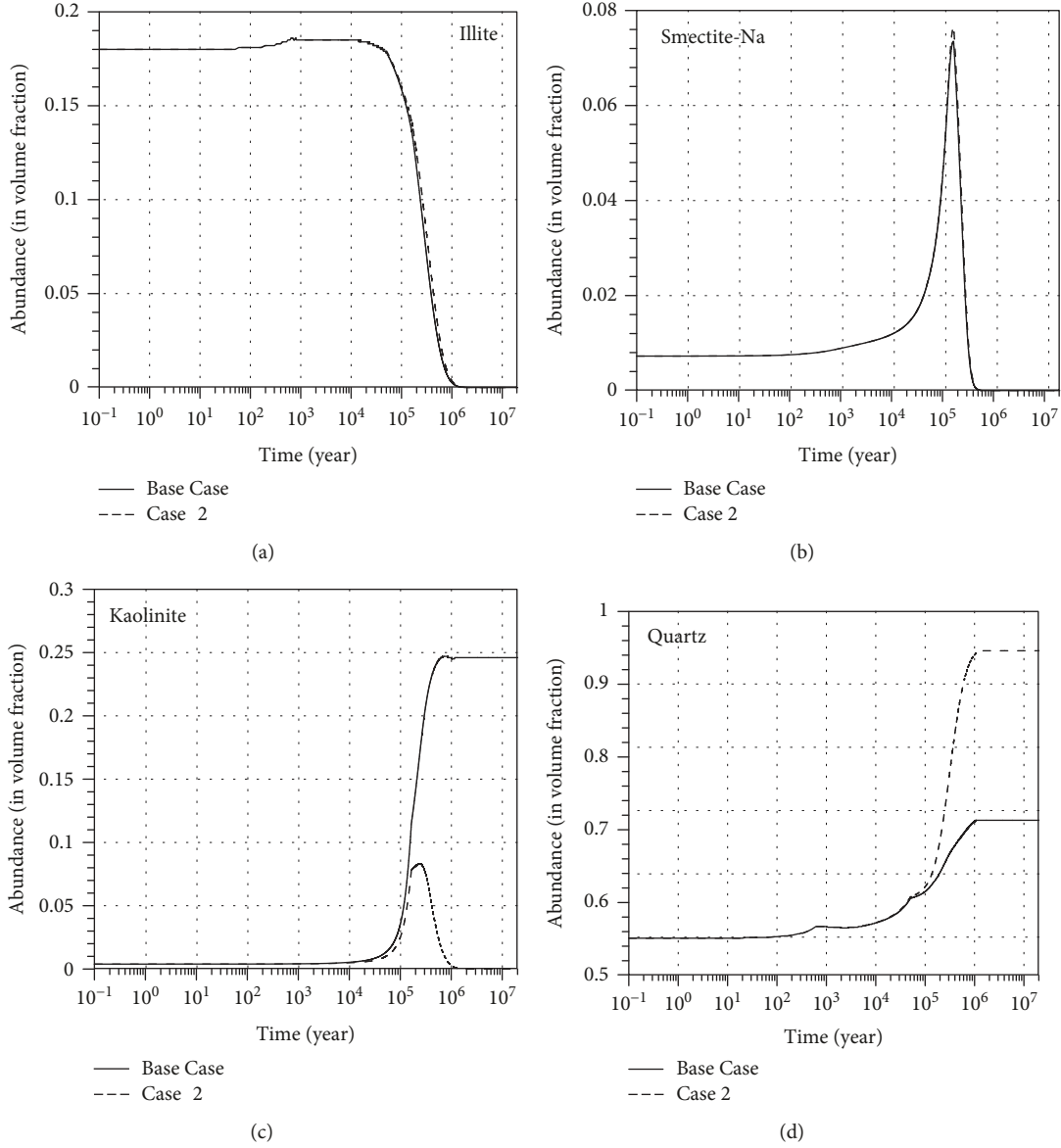
FIGURE 7: Variations in abundance (in volume fraction of rock grains) of illite (a), smectite-Na (b), kaolinite (c), and quartz (d) versus time obtained with (Case 2) and without (Base Case) considering the scour of kaolinite.

new function must be added to the existing program manually. For simplicity, we introduced a coefficient of scour (Sco) for a mineral to describe the erosion process of the mineral. The resulting equation is as follows:

$$\mathrm{fr}_m^{t+1} = \mathrm{fr}_m^t \times (1 - \mathrm{Sco}_m)^n, \tag{3}$$

where fr_m^t and fr_m^{t+1} are the volume fractions of the m-th mineral at times t and $t + 1$, respectively; Sco_m is the coefficient of scour of the m-th mineral and represents the proportion of mineral m that is washed away each year (in this study, it is set to 0.95×10^{-5} for kaolinite through trial and error); and n is the length of the current time step in years.

The scour of minerals affects the variation in porosity. These variations can be evaluated using equation (2).

The updated volume fraction fr_m^{t+1} of mineral m obtained in equation (3) is used in equation (2) for the calculation of porosity influenced by precipitation/dissolution and possible scour of minerals. Only the scour of kaolinite is assumed to have taken place in the Huangqiao area. To examine its effects on the mineral composition and porosity changes in the Longtan sandstone Formation, an additional simulation (i.e., Case 2) was performed by taking into account the scour of kaolinite in the Base Case.

Variations in the mineral composition and rock porosity of these 2 sets of simulations (i.e., Base Case and Case 2) are shown in Figures 7 and 8, respectively. It should be noted that to maintain consistency with the measured data in Table 1; the mineral abundances presented in Figure 8 are expressed in the volume fraction of rock grain (the ratio between the volume fraction of medium and volume fraction of rock
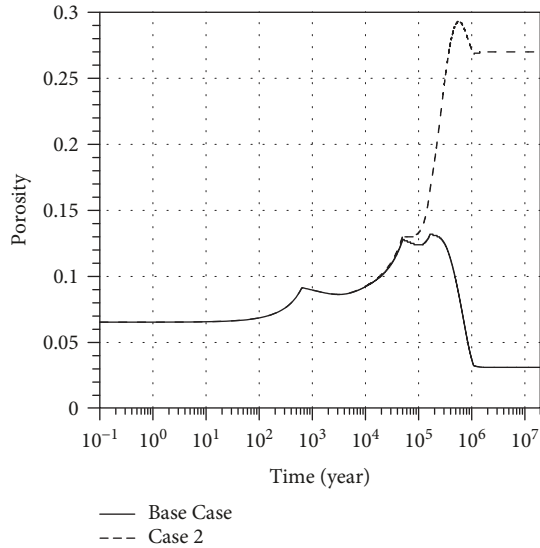
FIGURE 8: Variation in the porosity of the rock versus time obtained with (Case 2) and without (Base Case) considering the scour of kaolinite.

grain is (1-porosity)). Considering that fluid flow in the deep subsurface is generally very slow, the erosion rate of kaolinite would be very small, and it would take thousands of years or more to affect the mineral composition and rock porosity. Here, the coefficient of scour of kaolinite is set equal to 0.95×10^{-5} heuristically after a number of trial calculations. The scour of kaolinite would decrease the volume of kaolinite, thereby affecting the rock porosity and abundance of minerals.

As shown in Figure 7(c), it takes nearly 100,000 years to show a significant difference between the two cases with and without consideration of the scour of kaolinite when chlorite, feldspar, and carbonate minerals are completely dissolved. The simulation results show that the scour of kaolinite does not affect the abundance of illite (Figure 7(a)) and smectite-Na (Figure 7(b)). Affected by erosion, the abundance of kaolinite (Figure 7(c)) decreases significantly and decreases to zero after approximately 1 Ma. Consequently, the abundance of quartz (Figure 7(d)) increases prominently, and quartz becomes the dominant mineral of the rock.

The pore space becomes larger as the kaolinite is washed away by fluid flow. As shown in Figure 8, the simulated rock porosity in Case 2 increases significantly due to the scour of kaolinite between 50,000 and 600,000 years, with a maximum porosity of 29.3%. After 600,000 years, the joint effects of mineral dissolution/precipitation and scour of kaolinite decrease the pores of the host rock to some extent, and the porosity of the sandstone is approximately 27% after 1 Ma.

As mentioned above, CO_2 is proposed to have invaded the Longtan sandstone Formation at approximately 20 Ma. However, the exact duration of the CO_2-brine-rock interaction is difficult to determine because it stops once the water has been drained by CO_2. By comparing the simulation results with the measured data for samples from Well X3 (i.e., the natural analogue), we find that the mineral assemblage in Case 2 after approximately 500,000 years fits well

with the measured data (as shown in Figure 9). The simulated mineral composition at this time point consists of 87.5% quartz, 3.3% kaolinite, 3.7% illite, and 0.02% smectite. The simulated abundance of quartz lies within the observed range (85.7~89.1%) of sandstone samples from Well X3, and that of kaolinite is slightly higher than the measured data (1.7~2.8%). The simulated volume fraction of illite fits well with the measured data while that of smectite is slightly smaller than the measured data. In addition, the simulated porosity in Case 2 after 500,000 years is 29%, while the measured average porosity of sandstone samples from Well X3 is approximately 15%. The simulated porosity in the Base Case is approximately 9% after 500,000 years and decreases as the reaction continues, which is inconsistent with the field observations. Therefore, the simulated changes in porosity give us more confidence that the scour of kaolinite has occurred in this area and affected the mineral composition and porosity variation of the rock, although the simulated rock porosity and abundance of kaolinite in the revised model (i.e., Case 2) are higher than the measured data. The simulated main evolution trends of minerals are consistent with field observations, including the complete dissolution of chlorite, carbonate, and feldspar minerals and the precipitation of kaolinite and paragenetic quartz. Given the complexity of the long-term geochemical reactions and the variety of factors that may impact, we deem that these deviations between simulation results and measured data are tolerable and that the revised model (Case 2) can reproduce the process of long-term CO_2-water-rock interaction in the Longtan sandstone Formation in the Huangqiao area.

7. Summary and Conclusions

A one-dimensional reactive transport model of CO_2 intrusion into the Longtan sandstone Formation was constructed, and the alteration patterns of minerals and changes in porosity for the sandstone induced by the intrusion of CO_2 over a long time scale (20 Ma) were investigated. The simulation results were calibrated using the measured mineralogical and physical data for sandstone cores from Well X3, and the following conclusions can be drawn.

The geochemical processes induced by the intrusion of CO_2 can be roughly divided into two stages. First, the flooding of CO_2 decreases the pH of the solution, resulting in the dissolution of some susceptible minerals (e.g., chlorite, calcite, ankerite, and feldspars). The dissolution of chlorite and ankerite supplies Fe^{2+} for the precipitation of siderite. Dawsonite and smectite-Ca form with the dissolution of albite and anorthite, respectively. Dawsonite begins to transform into smectite-Na after albite is completely dissolved. K-feldspar converts into illite with Mg^{2+} provided by the dissolution of chlorite. Second, as the reactions continue, intermediate products (i.e., illite, smectite-Na, and smectite-Ca) generated in the first stage become the reactants and subsequently react with CO_2 and brine. Kaolinite and quartz are the final products of geochemical reactions.

Compared with the field data, the abundance of kaolinite simulated in the Base Case is much higher. By taking into account the scour of kaolinite in the simulation (i.e., Case
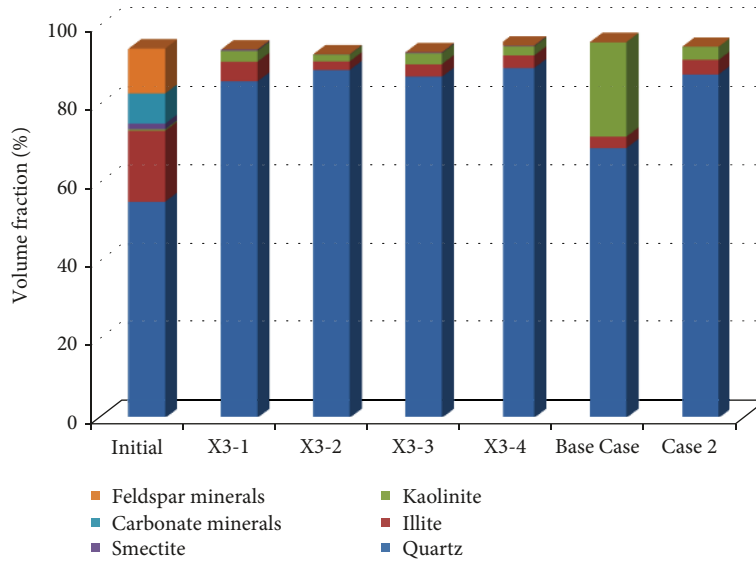
FIGURE 9: Comparison of the initial mineral assemblage of sandstone in the model, measured mineral assemblages of sandstone samples from Well X3 (X3-1, X3-2, X3-3, and X3-4), and simulated mineral assemblages of Base Case and Case 2 after 500,000 years. The simulation results show that the main brine-rock reactions induced by CO_2 include the dissolution of feldspar minerals and carbonate minerals and the precipitation of quartz and kaolinite.

TABLE 5: List of kinetic rate parameters used in equations (A.1) and (A.2) for minerals considered in the simulations.

| Mineral | A (cm^2/g) | Parameters for kinetic rate law of equations (A.1) and (A.2) | | | | | | | |
| | | Neutral mechanism | | Acid mechanism | | | Base mechanism | | |
		k_{25} (mol/m^2/s)	E_a (KJ/mol)	k_{25} (mol/m^2/s)	E_a (KJ/mol)	$n(H^+)$	k_{25} (mol/m^2/s)	E_a (KJ/mol)	$n(H^+)$
Quartz	9.8	1.023×10^{-14}	87.7						
Illite	151.6	1.660×10^{-13}	35	1.047×10^{-11}	23.6	0.34	2.020×10^{-17}	58.9	-0.4
Kaolinite	151.6	6.918×10^{-14}	22.2	4.898×10^{-12}	65.9	0.777	8.913×10^{-18}	17.9	-0.472
Chlorite	9.8	3.02×10^{-13}	88	7.762×10^{-12}	88	0.5			
Smectite-Na	151.6	1.660×10^{-13}	35	1.047×10^{-11}	22.6	0.34	2.020×10^{-17}	58.9	-0.4
Smectite-Ca	151.6	1.660×10^{-13}	35	1.047×10^{-11}	22.6	0.34	2.020×10^{-17}	58.9	-0.4
Albite	9.8	2.754×10^{-13}	69.8	6.918×10^{-11}	65	0.457	2.512×10^{-16}	71	-0.572
Anorthite	10.0	7.586×10^{-13}	17.8	3.162×10^{-4}	16.6	1.411			
K-feldspar	9.8	2.890×10^{-13}	38	8.710×10^{-11}	51.7	0.5	6.310×10^{-22}	94.1	-0.823
Calcite	9.8	1.549×10^{-6}	23.5	5.012×10^{-4}	14.4	1.0			
Ankerite	9.8	1.260×10^{-9}	62.76	6.457×10^{-4}	36.1	0.5			
Siderite	9.8	1.260×10^{-9}	62.76	6.457×10^{-4}	36.1	0.5			
Dolomite	9.8	2.951×10^{-8}	52.2	6.457×10^{-4}	36.1	0.5			
Dawsonite	9.8	1.260×10^{-9}	62.76	6.457×10^{-4}	36.1	0.5			
Magnesite	9.8	4.571×10^{-10}	23.5	4.169×10^{-7}	14.4	1			
Nonreactive									

2), the simulated volume fractions of quartz and illite after approximately 500,000 years fit well with the measured data for samples taken from Well X3 in the Huangqiao CO_2 gas field (i.e., the natural analogue). We also find that the joint effects of CO_2-water-rock interactions and scour of kaolinite increase the porosity of the host rock, which is consistent with field observations. Therefore, the scour of kaolinite is likely to have occurred in this area and significantly affected the mineral composition and variation in porosity of the rock.

Further investigation is still required, especially using 2D or 3D models, to fully elucidate the geochemical and physical

processes associated with the intrusion of CO_2 into the sandstone formation. The range of problems concerning CO_2-brine-rock interactions is very broad, and the present simulation results are specific to the parameters and conditions considered. Given the need and the general inadequacy of other reliable methods to predict the long-term interactions of CO_2-brine-rock and reservoir responses, the combination of numerical modeling and natural analogue study would greatly facilitate and promote our understanding.

Appendix

A.Kinetic and Thermodynamic Parameters

Both equilibrium and kinetic mineral dissolution/precipitation can be simulated in TOUGHREACT. Considering the sluggish nature of the CO_2-brine-rock reactions, kinetic formulations are used for all the mineral-water reactions in the model. For kinetically controlled mineral dissolution and precipitation, a general form of the rate law [57, 58] is used.

$$r_n = \pm k_n A_n \left| 1 - \Omega_n^\theta \right|^\eta, \tag{A.1}$$

where the subscript n denotes the kinetic mineral index, r_n is the dissolution/precipitation rate of the mineral (positive values indicate dissolution, and negative values indicate precipitation), k_n is the rate constant that is temperature dependent, A_n is the specific reactive surface area per kg H_2O, and Ω_n is the kinetic mineral saturation ratio. The superscripts θ and η must be determined from experiments; usually, but not always, they are taken as equal to one.

The dissolution and precipitation of minerals are often catalyzed by H^+ and OH^-. Therefore, for many minerals, the kinetic rate constant k includes three mechanisms (i.e., acid, neutral, and base mechanisms) [59, 60] or

$$
\begin{aligned}
k = \; & k_{25}^{\mathrm{nu}} \exp\left[\frac{-E_a^{\mathrm{nu}}}{R}\left(\frac{1}{T} - \frac{1}{298.15}\right)\right] \\
& + k_{25}^{\mathrm{H}} \exp\left[\frac{-E_a^{\mathrm{H}}}{R}\left(\frac{1}{T} - \frac{1}{298.15}\right)\right] a_{\mathrm{H}}^{n_{\mathrm{H}}} \\
& + k_{25}^{\mathrm{OH}} \exp\left[\frac{-E_a^{\mathrm{OH}}}{R}\left(\frac{1}{T} - \frac{1}{298.15}\right)\right] a_{\mathrm{OH}}^{n_{\mathrm{OH}}},
\end{aligned}
\tag{A.2}
$$

where superscripts or subscripts nu, H, and OH indicate neutral, acid, and base mechanisms, respectively; k_{25} is the rate constant at 25°C; a is the activity of the species; n is the power term (constant); R is the gas constant; and T is the absolute temperature. The parameters for the kinetic rate calculation of specific minerals are similar to those used by Xu et al. [19], which were derived from Palandri and Kharaka [59] (see Table 5).

The thermodynamic data for aqueous species, gases, and minerals were mostly taken from the built-in database of TOUGHREACT, i.e., the EQ3/6 V7.2b database [61], as previously done by Xu et al. [28, 36] and Tian et al. [45].

Data Availability

The underlying data can be provided if necessary by the corresponding author upon request.

Conflicts of Interest

The authors declares that they have no conflicts of interest.
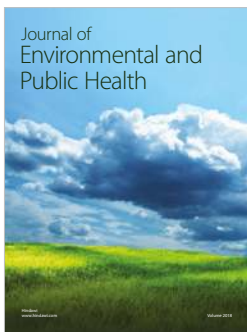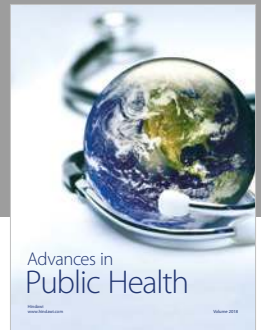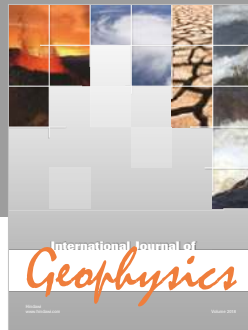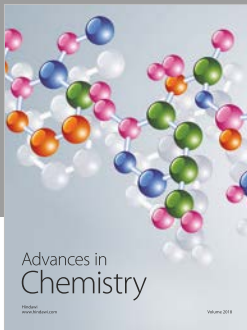
Acknowledgments

References

[1] B. Metz, O. Davidson, H. D. Coninck, and L. Meyer, *IPCC Special Report on Carbon dioxide Capture and Storage: Cost and economic potential*, Cambridge University Press, Cambidge, England, 2005.

[2] C. A. Hendriks and K. Blok, "Underground storage of carbon dioxide," *Energy Conversion and Management*, vol. 36, no. 6-9, pp. 539–542, 1995.

[3] M. Wigand, J. W. Carey, H. Schütt, E. Spangenberg, and J. Erzinger, "Geochemical effects of CO_2 sequestration in sandstones under simulated in situ conditions of deep saline aquifers," *Applied Geochemistry*, vol. 23, no. 9, pp. 2735–2745, 2008.

[4] H. G. Koide, Y. Tazaki, Y. Noguchi, M. Iijima, K. Ito, and Y. Shindo, "Carbon dioxide injection into useless aquifers and recovery of natural gas dissolved in fossil water," *Energy Conversion and Management*, vol. 34, no. 9-11, pp. 921–924, 1993.

[5] R. G. Bruant, A. J. Guswa, M. A. Celia, and C. A. Peters, "Safe storage of CO_2 in deep saline aquifers," *Environmental Science & Technology*, vol. 36, no. 11, pp. 240A–245A, 2002.

[6] I. Gaus, P. Audigane, L. André et al., "Geochemical and solute transport modelling for CO_2 storage, what to expect from it?," *International Journal of Greenhouse Gas Control*, vol. 2, no. 4, pp. 605–625, 2008.

[7] R. Shukla, P. G. Ranjith, S. K. Choi, A. Haque, M. Yellishetty, and L. Hong, "Mechanical behaviour of reservoir rock under brine saturation," *Rock Mechanics and Rock Engineering*, vol. 46, no. 1, pp. 83–93, 2013.

[8] T. D. Rathnaweera, P. G. Ranjith, M. S. A. Perera et al., "CO_2-induced mechanical behaviour of Hawkesbury sandstone in the Gosford basin: an experimental study," *Materials Science and Engineering: A*, vol. 641, pp. 123–137, 2015.

[9] T. D. Rathnaweera, P. G. Ranjith, M. S. A. Perera et al., "An experimental investigation of coupled chemico-mineralogical and mechanical changes in varyingly-cemented sandstones upon CO_2 injection in deep saline aquifer environments," *Energy*, vol. 133, pp. 404–414, 2017.

[10] P. Bertier, R. Swennen, B. Laenen, D. Lagrou, and R. Dreesen, "Experimental identification of CO_2–water–rock interactions caused by sequestration of CO_2 in Westphalian and Buntsandstein sandstones of the Campine Basin (NE-Belgium),"

Journal of Geochemical Exploration, vol. 89, no. 1-3, pp. 10–14, 2006.

[11] J. P. Kaszuba, D. R. Janecky, and M. G. Snow, "Carbon dioxide reaction processes in a model brine aquifer at 200°C and 200 bars: implications for geologic sequestration of carbon," *Applied Geochemistry*, vol. 18, no. 7, pp. 1065–1080, 2003.

[12] R. J. Rosenbauer, T. Koksalan, and J. L. Palandri, "Experimental investigation of CO_2–brine–rock interactions at elevated temperature and pressure: implications for CO_2 sequestration in deep-saline aquifers," *Fuel Processing Technology*, vol. 86, no. 14-15, pp. 1581–1597, 2005.

[13] S. M. Farquhar, J. K. Pearce, G. K. W. Dawson et al., "A fresh approach to investigating CO_2 storage: experimental CO_2–water–rock interactions in a low-salinity reservoir system," *Chemical Geology*, vol. 399, pp. 98–122, 2015.

[14] C. Dalkhaa, M. Shevalier, M. Nightingale, and B. Mayer, "2-D reactive transport modeling of the fate of CO_2 injected into a saline aquifer in the Wabamun Lake Area, Alberta, Canada," *Applied Geochemistry*, vol. 38, pp. 10–23, 2013.

[15] W. D. Gunter, B. Wiwehar, and E. H. Perkins, "Aquifer disposal of CO_2-rich greenhouse gases: extension of the time scale of experiment for CO_2-sequestering reactions by geochemical modelling," *Mineralogy and Petrology*, vol. 59, no. 1-2, pp. 121–140, 1997.

[16] D. Li, S. Bauer, K. Benisch, B. Graupner, and C. Beyer, "OpenGeoSys-ChemApp: a coupled simulator for reactive transport in multiphase systems and application to CO_2 storage formation in Northern Germany," *Acta Geotechnica*, vol. 9, no. 1, pp. 67–79, 2014.

[17] F. Liu, P. Lu, C. Zhu, and Y. Xiao, "Coupled reactive flow and transport modeling of CO_2 sequestration in the Mt. Simon sandstone formation, Midwest U.S.A.," *International Journal of Greenhouse Gas Control*, vol. 5, no. 2, pp. 294–307, 2011.

[18] W. Zhang, Y. Li, T. Xu, H. Cheng, Y. Zheng, and P. Xiong, "Long-term variations of CO_2 trapped in different mechanisms in deep saline formations: a case study of the Songliao Basin, China," *International Journal of Greenhouse Gas Control*, vol. 3, no. 2, pp. 161–180, 2009.

[19] T. Xu, J. A. Apps, K. Pruess, and H. Yamamoto, "Numerical modeling of injection and mineral trapping of CO_2 with H_2S and SO_2 in a sandstone formation," *Chemical Geology*, vol. 242, no. 3-4, pp. 319–346, 2007.

[20] L. Yang, T. Xu, G. Feng et al., "CO_2-induced geochemical reactions in heterogeneous sandstone and potential conditions causing the tight cementation," *Applied Geochemistry*, vol. 80, pp. 14–23, 2017.

[21] J. M. Pearce, S. Holloway, H. Wacker, M. K. Nelis, C. Rochelle, and K. Bateman, "Natural occurrences as analogues for the geological disposal of carbon dioxide," *Energy Conversion & Management*, vol. 37, no. 6-8, pp. 1123–1128, 1996.

[22] N. Kampman, M. J. Bickle, A. Maskell et al., "Drilling and sampling a natural CO_2 reservoir: implications for fluid flow and CO_2-fluid–rock reactions during CO_2 migration through the overburden," *Chemical Geology*, vol. 369, pp. 51–82, 2014.

[23] Z. Zhou, C. J. Ballentine, M. Schoell, and S. H. Stevens, "Identifying and quantifying natural CO_2 sequestration processes over geological timescales: the Jackson Dome CO_2 deposit, USA," *Geochimica Et Cosmochimica Acta*, vol. 86, pp. 257–275, 2012.

[24] K. E. Higgs, R. R. Haese, S. D. Golding, U. Schacht, and M. N. Watson, "The Pretty Hill Formation as a natural analogue for CO_2 storage: an investigation of mineralogical and isotopic changes associated with sandstones exposed to low, intermediate and high CO_2 concentrations over geological time," *Chemical Geology*, vol. 399, pp. 36–64, 2015.

[25] N. Kampman, M. Bickle, M. Wigley, and B. Dubacq, "Fluid flow and CO_2–fluid–mineral interactions during CO_2-storage in sedimentary basins," *Chemical Geology*, vol. 369, pp. 22–50, 2014.

[26] V. N. Balashov, G. D. Guthrie, J. A. Hakala, C. L. Lopano, J. D. Rimstidt, and S. L. Brantley, "Predictive modeling of CO_2 sequestration in deep saline sandstone reservoirs: impacts of geochemical kinetics," *Applied Geochemistry*, vol. 30, pp. 41–56, 2013.

[27] N. Kampman, P. Bertier, A. Busch et al., "Validating reactive transport models of CO_2-brine-rock reactions in caprocks using observations from a natural CO_2 reservoir," *Energy Procedia*, vol. 114, pp. 4902–4916, 2017.

[28] T. Xu, H. Zhu, G. Feng, Z. Yang, and H. Tian, "Numerical simulation of calcite vein formation and its impact on caprock sealing efficiency- case study of a natural CO_2 reservoir," *International Journal of Greenhouse Gas Control*, vol. 83, pp. 29–42, 2019.

[29] R. S. Haszeldine, O. Quinn, G. England et al., "Natural geochemical analogues for carbon dioxide storage in deep geological porous reservoirs, a United Kingdom perspective," *Oil & Gas Science and Technology*, vol. 60, no. 1, pp. 33–49, 2005.

[30] N. Liu, L. Liu, X. Y. Qu, H. D. Yang, L. J. Wang, and S. Zhao, "Genesis of authigene carbonate minerals in the Upper Cretaceous reservoir, Honggang Anticline, Songliao Basin: a natural analog for mineral trapping of natural CO_2 storage," *Sedimentary Geology*, vol. 237, no. 3-4, pp. 166–178, 2011.

[31] J. Moore, M. Adams, R. Allis, S. Lutz, and S. Rauzi, "Mineralogical and geochemical consequences of the long-term presence of CO_2 in natural reservoirs: an example from the Springerville–St. Johns Field, Arizona, and New Mexico, U.S.A.," *Chemical Geology*, vol. 217, no. 3-4, pp. 365–385, 2005.

[32] J. Pearce, I. Czernichowski-Lauriol, S. Lombardi et al., "A review of natural CO_2 accumulations in Europe as analogues for geological sequestration," *Geological Society, London, Special Publications*, vol. 233, no. 1, pp. 29–41, 2004.

[33] M. N. Watson, N. Zwingmann, and N. M. Lemon, "The Ladbroke Grove–Katnook carbon dioxide natural laboratory: a recent CO_2 accumulation in a lithic sandstone reservoir," *Energy*, vol. 29, no. 9-10, pp. 1457–1466, 2004.

[34] I. Gaus, C. L. Guern, J. Pearce et al., "Comparison of long-term geochemical interactions at two natural CO_2-analogues: Montmiral (Southeast Basin, France) and Messokampos (Florina Basin, Greece) case studies. Greenhouse Gas Control Technologies 7," in *Proceedings of the 7th International Conference on Greenhouse Gas Control Technologies 5*, pp. 561–569, Vancouver, Canada, September 2005.

[35] Q. Ren, W. Hu, X. Wang et al., "Experimental study of the fluid-rock interactions between CO_2-rich fluid and sandstone and its application: a case study of the upper Longtan Formation in the Huangqiao oil and gas reservoir," *Geological Journal of China Universities (in chinese)*, vol. 23, pp. 134–147, 2017.

[36] T. Xu, J. A. Apps, and K. Pruess, "Mineral sequestration of carbon dioxide in a sandstone–shale system," *Chemical Geology*, vol. 217, no. 3-4, pp. 295–318, 2005.

[37] H. Ge and Z. Zhang, "Effect of magmatic hydrothermal on gas reservoir formation in Permian-Lower Triassic source rocks in Huangqiao Area, South China," *Geosystem Engineering*, vol. 19, no. 6, pp. 275–283, 2016.

[38] Q. Liu, D. Zhu, Z. Jin, Q. Meng, X. Wu, and H. Yu, "Effects of deep CO_2 on petroleum and thermal alteration: the case of the Huangqiao oil and gas field," *Chemical Geology*, vol. 469, pp. 214–229, 2017.

[39] J. Dai, S. Yang, H. Chen, and X. Shen, "Geochemistry and occurrence of inorganic gas accumulations in Chinese sedimentary basins," *Organic Geochemistry*, vol. 36, no. 12, pp. 1664–1688, 2005.

[40] S. Cui, *Tight sandstone reservoir assessment of Longtanzu Formation*, China University of Petroleum (EastChina), 2015.

[41] P. F. Boulin, P. Bretonnier, V. Vassil, A. Samouillet, M. Fleury, and J. M. Lombard, "Sealing efficiency of caprocks: experimental investigation of entry pressure measurement methods," *Marine and Petroleum Geology*, vol. 48, pp. 20–30, 2013.

[42] C. Sy, *Reservoir characteristics and petroleum accumulation of Permian Longtan Formation in Xiqiao tectonic belt of Huangqiao region, Lower Yangtze Basinbasin*, Nanjing University, 2014.

[43] T. Xu, N. Spycher, E. Sonnenthal, G. Zhang, L. Zheng, and K. Pruess, "TOUGHREACT version 2.0: a simulator for subsurface reactive transport under non-isothermal multiphase flow conditions," *Computers & Geosciences*, vol. 37, no. 6, pp. 763–774, 2011.

[44] L. André, P. Audigane, M. Azaroual, and A. Menjoz, "Numerical modeling of fluid–rock chemical interactions at the supercritical CO_2 – liquid interface during CO_2 injection into a carbonate reservoir, the Dogger aquifer (Paris Basin, France)," *Energy Conversion and Management*, vol. 48, no. 6, pp. 1782–1797, 2007.

[45] H. Tian, T. Xu, F. Wang, V. V. Patil, Y. Sun, and G. Yue, "A numerical study of mineral alteration and self-sealing efficiency of a caprock for CO_2 geological storage," *Acta Geotechnica*, vol. 9, no. 1, pp. 87–100, 2014.

[46] T. Xu, L. Zheng, and H. Tian, "Reactive transport modeling for CO_2 geological sequestration," *Journal of Petroleum Science & Engineering*, vol. 78, no. 3-4, pp. 765–777, 2011.

[47] K. Pruess, C. Oldenburg, and G. Moridis, *TOUGH2 User's Guide Version 2.0. Report LBNL-43134*, Lawrence Berkeley National Laboratory, Berkeley, CA, USA, 1999.

[48] J. M. Ketzer, R. Iglesias, S. Einloft, J. Dullius, R. Ligabue, and V. de Lima, "Water–rock–CO_2 interactions in saline aquifers aimed for carbon dioxide storage: experimental and numerical modeling studies of the Rio Bonito Formation (Permian), southern Brazil," *Applied Geochemistry*, vol. 24, no. 5, pp. 760–767, 2009.

[49] S. P. White, R. G. Allis, J. Moore et al., "Simulation of reactive transport of injected CO_2 on the Colorado Plateau, Utah, USA," *Chemical Geology*, vol. 217, no. 3-4, pp. 387–405, 2005.

[50] W. Fu, "Influence of clay minerals on sandstone reservoir prooerties," *Journal of Palaeogegrphy*, vol. 2, pp. 59–68, 2000.

[51] G. Zhu, "Effects of clay minerals on the Triassic sandstone reservoir in Shan-Gan-Ning Basin and their significance," *Petroleum Exploration and Development*, vol. 4, pp. 20–29, 1988.

[52] J. Cao, Y. Zhang, and W. Hu, "Developing characteristics of kaolinite in central Junggar Basin and their effect on the reservoir quality," *Acta Mineralogica Sinica*, vol. 25, pp. 367–373, 2005.

[53] F. Civan, "Reservoir formation damage: fundamentals, modeling, assessment, and mitigation," *Herd Health Environments Research & Design Journal*, vol. 7, pp. 60–77, 2000.

[54] K. C. Khilar, *Migrations of Fines in Porous Media*, Kluwer Academic Publishers, 1998.

[55] S. F. Kia, H. S. Fogler, M. G. Reed, and R. N. Vaidya, "Effect of salt composition on clay release in Berea sandstones," *SPE Production Engineering*, vol. 2, no. 4, pp. 277–283, 1987.

[56] T. Russell, D. Pham, M. T. Neishaboor et al., "Effects of kaolinite in rocks on fines migration," *Journal of Natural Gas Science and Engineering*, vol. 45, pp. 243–255, 2017.

[57] A. C. Lasaga, "Chemical kinetics of water-rock interactions," *Journal of Geophysical Research Solid Earth.*, vol. 89, no. B6, pp. 4009–4025, 1984.

[58] C. I. Steefel and A. C. Lasaga, "A coupled model for transport of multiple chemical-species and kinetic precipitation dissolution reactions with application to reactive flow in single-phase hydrothermal systems," *American Journal of Science*, vol. 294, no. 5, pp. 529–592, 1994.

[59] J. L. Palandri and Y. K. Kharaka, *A compilation of rate parameters of water-mineral interaction kinetics for application to geochemical modeling*, U.S. Geological Surver, Menlo Park, CA, USA, 2004.

[60] A. C. Lasaga, J. M. Soler, J. Ganor, T. E. Burch, and K. L. Nagy, "Chemical weathering rate laws and global geochemical cycles," *Geochimica et Cosmochimica Acta*, vol. 58, no. 10, pp. 2361–2386, 1994.

[61] T. J. Wolery, *EQ3/6, a software package for geochemical modeling of aqueous systems: package overview and installation guide (version 7.0)*, Office of Scientific & Technical Information Technical Reports, 1992.

Advances in
Chemistry

Scientifica

International Journal of
Geophysics

The Scientific World Journal

Advances in
Public Health

Journal of
Environmental and Public Health

Advances in
Meteorology

Applied & Environmental Soil Science

Journal of
Geological Research

International Journal of
Forestry Research

International Journal of
Agronomy

International Journal of
Microbiology

International Journal of
Ecology

Advances in
Agriculture

International Journal of
Biodiversity

Archaea

International Journal of
Analytical Chemistry

Journal of
Chemistry

Journal of
Marine Biology

Hindawi

Submit your manuscripts at
www.hindawi.com